The Astrophysical Journal, 890:96 (13pp), 2020 February 20 https://doi.org/10.3847/1538-4357/ab6664

Penumbral Brightening Events Observed in AR NOAA 12546

Mariarita Murabito[1], Salvo L. Guglielmino[2], Ilaria Ermolli[1], Marco Stangalini[1,3], and Fabrizio Giorgi[1]
[1] INAF—Osservatorio Astronomico di Roma, Via Frascati, 33, Roma Italy; mariarita.murabito@inaf.it
[2] Dipartimento di Fisica e Astronomia—Sezione Astrofisica, Università degli Studi di Catania, Via S. Sofia 78, I-95123 Catania, Italy
[3] ASI, Agenzia Spaziale Italiana, Via del Politecnico snc, I-00133 Rome, Italy
Received 2019 October 31; revised 2019 December 4; accepted 2019 December 4; published 2020 February 17

Abstract

Penumbral transient brightening events have been attributed to magnetic reconnection episodes occurring in the low corona. We investigated the trigger mechanism of these events in active region NOAA 12546 by using multiwavelength observations obtained with the Interferometric Bidimensional Spectrometer, by the *Solar Dynamics Observatory*, the *Interface Region Imaging Spectrograph*, and the *Hinode* satellites. We focused on the evolution of an area of the penumbra adjacent to two small-scale emerging flux regions (EFRs), which manifested three brightening events detected from the chromosphere to the corona. Two of these events correspond to B-class flares. The same region showed short-lived moving magnetic features (MMFs) that streamed out from the penumbra. In the photosphere, the EFRs led to small-scale penumbral changes associated with a counter-Evershed flow and to a reconfiguration of the magnetic fields in the moat. The brightening events had one of the footpoints embedded in the penumbra and seemed to result from the distinctive interplay between the preexisting penumbral fields, MMFs, and the EFRs. The *IRIS* spectra measured therein reveal enhanced temperature and asymmetries in spectral lines, suggestive of event triggering at different heights in the atmosphere. Specifically, the blue asymmetry noted in C II and Mg II h&k lines suggests the occurrence of chromospheric evaporation at the footpoint located in the penumbra as a consequence of the magnetic reconnection process at higher atmospheric heights.

Unified Astronomy Thesaurus concepts: Solar magnetic reconnection (1504); Solar magnetic fields (1503); Active solar chromosphere (1980); Solar photosphere (1518); Solar X-ray emission (1536)

Supporting material: animations

1. Introduction

Present-day high resolution observations reveal the dynamic fine scale structure of sunspots created by magnetoconvective interactions (Borrero & Ichimoto 2011; Rempel & Schlichenmaier 2011). Small-scale features in a sunspot (umbral and penumbral) vary in space and time due to a number of different processes. These include oscillations, waves, jets of plasma, and magnetic reconnection. This is believed to lead to flaring events. The latter phenomena involve plasma heating, particle acceleration, and the release of electromagnetic energy from X-rays to radio wavelengths (Shibata & Magara 2011; Benz 2017).

Smaller-scale energy release phenomena detected over and near sunspots' penumbrae have been related to new magnetic elements in emerging flux regions (EFRs, e.g., Guglielmino 2012; Cheung & Isobe 2014) and to magnetic features moving away from the sunspot toward the boundary of the moat region (moving magnetic features (MMFs), see, e.g., Criscuoli et al. 2012; Li et al. 2019, and references therein), which can cancel with preexisting magnetic fields.

In this regard, Kano et al. (2010) analyzed microflares around a well-developed sunspot, by using *Hinode* (Kosugi et al. 2007) satellite data from the X-ray Telescope (XRT; Golub et al. 2007) and the Narrowband Filter Imager mounted on the Solar Optical Telescope (Tsuneta et al. 2008). They found that half of the observed microflares were caused by magnetic flux cancellation (*encounters of opposite polarities* in their paper) and when the latter is the main cause, the microflare has one of the X-ray loops connecting the penumbra to the opposite polarity patch of an EFR or an MMF embedded in the moat.

Recently, Bai et al. (2016) reported on a penumbral transient brightening observed with state-of-the-art instruments installed in the *Interface Region Imaging Spectrograph* (*IRIS*, De Pontieu et al. 2014) satellite and the 1.6 m New Solar Telescope (Cao et al. 2010; Goode et al. 2010) at the Big Bear Solar Observatory. This penumbral brightening, whose estimated thermal energy was in the range of nanoflares (10^{22}–10^{25} erg), displayed signatures from the chromosphere to the corona. The same authors found that an MMF had appeared close to the penumbral boundary and at the same location of one of the footpoints associated with the observed brightening. Bai et al. (2016) attributed the triggering mechanism of the analyzed event to magnetic reconnection occurring in the low corona and explained the brightening seen in the transition region (TR) and chromosphere as due to the local plasma heated up by downward propagating accelerating particles and thermal conduction. However, due to very weak signals of the observations analyzed, those authors could not find any evidence of the chromospheric evaporation that is expected to follow the heating of the chromospheric plasma from reconnection processes in the low corona. This evaporation has been reported from analysis of larger flares (Tian et al. 2014; Graham & Cauzzi 2015), as well as in micro- (Chen & Ding 2010) and nanoflares (Testa et al. 2014) observed outside penumbrae. Since the trigger mechanism of the studied brightening could not be clearly identified by their analysis, Bai et al. (2016) solicited more research on the formation process of brightening events observed in penumbral regions.

Indeed, it is well known that the magnetic reconnection can occur on any spatial or temporal scale in the solar atmosphere (Priest & Forbes 2000). Both the current high resolution observations and magnetohydrodynamical (MHD) numerical simulations indicate that interactions of EFRs with preexisting ambient magnetic fields (Archontis 2012; Cheung & Isobe 2014; Schmieder et al. 2014) play a prominent role in models

of large- (e.g., Louis et al. 2015, and references therein) and small-scale eruptive events (e.g., Guglielmino et al. 2010, 2018, 2019, and references therein). In particular, it is expected that the magnetic reconnection can occur at different atmospheric heights depending on the overlying and/or background magnetic fields and on the strength and size of the EFR (Archontis et al. 2004; MacTaggart et al. 2015). Furthermore, Galsgaard et al. (2005, 2007) demonstrated that the magnetic reconnection strongly depends on the relative orientation between the magnetic field components of the emerging flux and the preexisting magnetic field. In fact, only when the two flux systems have almost antiparallel orientation is the magnetic reconnection efficient.

In this study, we analyzed multiwavelength observations of the active region (AR) NOAA 12546 obtained with state-of-the-art instruments to further investigate the trigger mechanism of penumbral brightening events. In particular, we studied the evolution of the penumbral area adjacent to two small-scale EFRs emerged in the AR on 2016 May 20. The analyzed region showed three brightening events detected from the chromosphere to the corona.

The paper is organized as follows: in the next Section we describe the observations and the data processing applied. In Section 3 we feature our analysis and results, which are summarized and discussed in Section 4. Section 5 presents our conclusions.

2. Data and Methods

2.1. Observations

We analyzed high spatial, spectral, and temporal resolution data acquired by the Interferometric Bidimensional Spectrometer (IBIS; Cavallini 2006) at the Dunn Solar Telescope of the National Solar Observatory, the Helioseismic and Magnetic Imager (HMI; Scherrer et al. 2012) and Atmospheric Imaging Assembly (AIA; Lemen et al. 2012) instruments on board the *Solar Dynamics Observatory* (*SDO*; Pesnell et al. 2012) satellite, and the *IRIS* and *Hinode*/XRT space-borne telescopes.

IBIS observations were carried out on 2016 May 20, when the AR was characterized by a β magnetic configuration. The data set consists of full-Stokes measurements taken along the Fe I 617.30 nm and Ca II 854.20 nm lines, each line sampled at 21 spectral positions over a field-of-view (FoV) of about $40'' \times 90''$. The data were acquired with a spectral sampling of 20 and 60 mÅ, and a spatial resolution of $0.16''$ and $0.23''$ for the Fe I and Ca II measurements, respectively, with a cadence of 48 s under excellent seeing conditions that lasted about 180 minutes (318 line scans). The data were processed with the methods described by, e.g., Ermolli et al. (2017). The same data set was also analyzed by Stangalini et al. (2018) and Murabito et al. (2019), to which we refer the reader for further details.

SDO data comprise the Space-weather HMI Active Region Patches (Bobra et al. 2014) continuum filtergrams, magnetograms, and Dopplergrams derived from the HMI measurements at the Fe I 617.3 nm line, performed with a resolution of $1''$ and a cadence of 12 minutes from 2016 May 19 at 08:00 UT to May 21 at 08:00 UT. Furthermore, we considered AIA filtergrams taken at the 1600, 304, 171, 335, and 131 Å bands (hereafter referred to as A1600, A304, A171, A335, and A131, respectively), with a pixel scale of about $0.6''$ and a cadence of 12 s and 24 s for the EUV and UV channels, respectively.

The *IRIS* data set was acquired at the time of the IBIS measurements on 2016 May 20 from 13:17 UT to 16:30 UT. It consists of a sit-and-stare scan (OBS362011063) taken with a cadence of 20 s at the C II 1334.53 Å, Si IV 1402.77 Å, and Mg II h&k 2796.35 and 2803.53 Å lines. Simultaneous slit-jaw filtergrams (SJIs) were acquired in the passbands of the Si IV 1400 Å line and Mg II k line wing (hereafter referred to as I1400 and I2832), with a cadence of 20 s and 97 s, respectively, covering an FoV of $120'' \times 119''$. The I1400 and I2832 data sample plasma at $T = 65{,}000$ K and $T = 6{,}000$–$10{,}000$ K, respectively.

Finally, we analyzed *Hinode*/XRT images taken through the Al polyimide and the Be thin filters, whose temperature response ranges $6 < \log T < 7.5$ for the former, and has a peak at $\sim\log T = 7$ for the latter (Golub et al. 2007). The two sets of images were acquired with a cadence of 60 s and varying exposure time. These data provide measurements over a FoV of $384'' \times 384''$, with a pixel size of $1.03''$. Note that XRT observations were taken simultaneously to *IRIS* data with some gaps.

2.2. Data Processing

We coaligned IBIS, *SDO*/HMI, and *SDO*/AIA observations by applying cross-correlation techniques on cospatial FoVs that were extracted from the three data sets. In particular, we used the first IBIS spectral image taken at the Fe I 617.3 nm line continuum on 2016 May 20 at 13:53 UT as a reference and the corresponding, neighboring-in-time *SDO*/HMI continuum image and *SDO*/AIA A1600 filtergram. We employed IDL *SolarSoft* mapping routines to account for the different pixel size of the data. Since the *SDO*/AIA data are aligned between them we employed the *SDO*/AIA A1600 image aligned to the IBIS data as a reference for the remaining *SDO*/AIA channels. Then, we aligned the *IRIS* data to the other measurements, by using the *IRIS* SJIs I2832 filtergrams and the closest in time *SDO*/HMI continuum images. Finally, we aligned the XRT images using the *SDO*/AIA A131 filtergrams as an anchor channel. The precision of our data alignment is comparable to the pixel size of the *SDO* observations, about $0.6''$, which is accurate enough for the analysis presented in the following.

To get quantitative estimates of the physical parameters in the analyzed region, we inverted the IBIS data by using the non-LTE inversion code NICOLE (Socas-Navarro et al. 2015). In brief, we assumed five equidistant nodes for temperature, three nodes for each component of the vector magnetic field (B_x, B_y, and B_z), two nodes for the line-of-sight (LOS) velocity, and one node for both the microturbulence and macroturbulence. We performed the inversions in two cycles, by assuming as the starting guess model a modified FALC atmosphere (Fontenla et al. 1993) with a constant value of 1.5 kG for B_z. We refer the reader to the paper by Murabito et al. (2019) for further details.

In order to study the horizontal proper motions and estimate the velocity of the photospheric plasma, we applied the Fourier Local Correlation Tracking technique (FLCT; Fisher & Welsch 2008) to the available *SDO*/HMI LOS magnetograms. We set the FWHM of the Gaussian tracking window to 15 pixels, in order to follow the collective motions of the

magnetic structures, and made a temporal integration over a time interval of 12 minutes.

In addition, we got pixelwise estimates of the LOS velocity of the photospheric plasma by computing the Doppler shift of the line core of the IBIS Fe I data with respect to the average position of the line core in a quiet Sun region. We computed the line core position by fitting the Stokes I Fe I measurements with a linear background and a Gaussian function.

3. Analysis and Results

From 2016 May 15 to 25, ground-based and space-borne solar telescopes detected the on-disk passage of AR NOAA 12546 (AR hereafter), which emerged in the southern solar hemisphere close to the equator. This AR consisted of a leading, large and almost circular sunspot and a trailing, extended plage region. The sunspot, which was one among the largest such structures observed over the solar cycle 24, kept its regular shape nearly unchanged during the disk passage, while the plage region evolved significantly. The studied sunspot also displayed a large number of MMFs, mostly of type II, i.e., unipolar features with the same polarity of spot (e.g., Zuccarello et al. 2009, and references therein), seen to move almost radially away from the sunspot structure toward the boundary of the moat region.

Both the *SDO*/HMI and IBIS photospheric observations show that the penumbra of AR was formed by bright filaments and dark spines nearly radially aligned over most of the sunspot structure (Murabito et al. 2019), except for an area close to the EFRs observed on 2016 May 20.

3.1. Magnetic Environment in the Photosphere

Figure 1 shows the region analyzed in our study as deduced from *SDO*/HMI continuum observation performed on 2016 May 19 at 13:34 UT and the region of interest (ROI) discussed in the following and shown in Figures 3, 6, and 7. The bottom panel of Figure 1 displays the LOS magnetogram with overplotted horizontal velocity.

Starting from 2016 May 19 12:00 UT the ROI showed in about 24 hr an increase of the LOS magnetic flux of about (2–4) $\times$ 10^{20} Mx for the positive and negative polarity, and a flux decrease afterwards. This flux variation, which is reported in Figure 2, followed the evolution of the region summarized in the panels of Figure 3, which show maps from *SDO*/HMI observations at 9 representative times from 2016 May 19 08:00 UT to May 21 00:00 UT.

On 2016 May 19 08:00 UT the ROI only included the southern sector of the penumbra and moat area nearby (Figure 3, first row). A few hours later, at 16:00 UT, negative polarity patches (labeled N in Figure 3, panel (b2)) from the new flux of an EFR emerging at $X = [20'', 50'']$, $Y = [15'', 40'']$, had already merged with preexisting network field forming a small pore and a few fainter structures (labeled N_1 and N_2 in Figure 3, panel (b3)). These structures also received the negative polarity flux from a second EFR appearing on 2016 May 20 01:00 UT. Thereafter, positive polarity patches streaming out from the penumbra and from the second EFR merged to form small-scale structures in the southeast section of the ROI (at $X = [5'', 30'']$, $Y = [10'', 25'']$) that later on, e.g., at 13:48 UT, were only merely discernible.

During the emergence of the second EFR, a bright lane (marked with red arrows in Figure 3, panels (a4)–(a5)) and a few dark patches (marked with the orange arrow in Figure 3, panel (a6)) appeared in the penumbra near the EFR, by creating a gap in the structure (see green arrows in Figure 3, panels (a4)–(a6)) that separated filaments with different orientation.

Later, the filaments closer to N_2 (black oval in Figure 3, panels (b7)–(b8)) broke away from the penumbra (black oval in Figure 3, panel (b8)) when the small-scale negative flux patches from the two EFRs and preexisting fields coalesced and got more aggregated (N_3 in Figure 3, panels (b7)–(b9)).

The animated version in Figure 3 (panels (a) and (b)), available in the online material clearly shows the entire

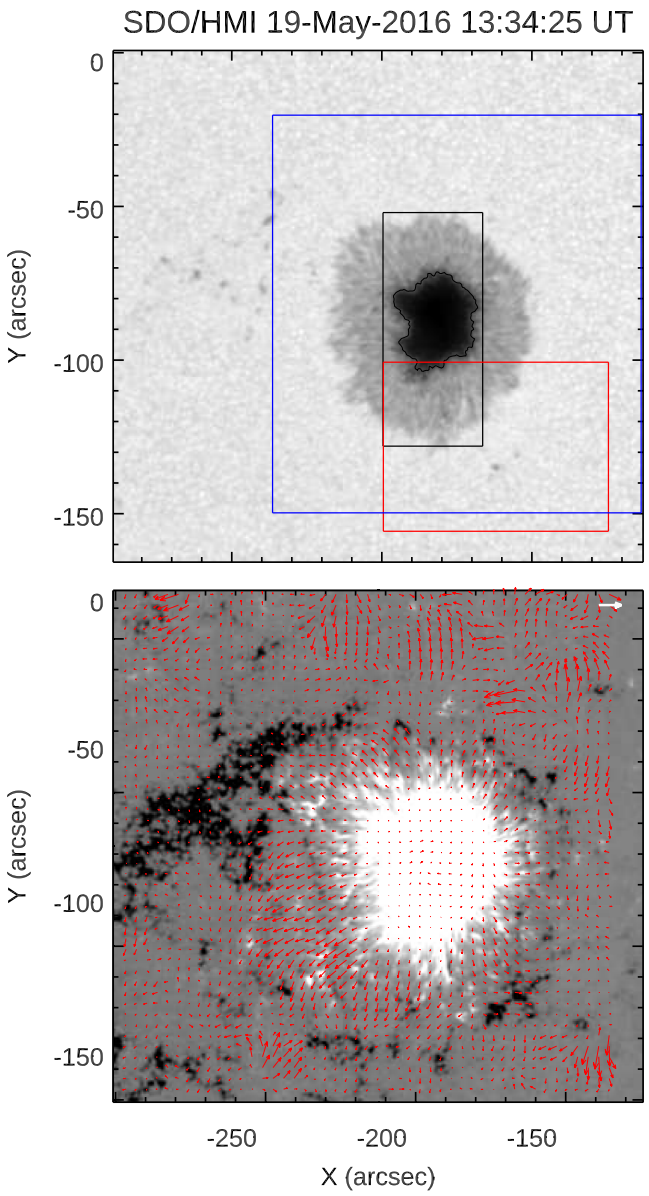

Figure 1. Subarray extracted from the full-disk continuum filtergram (top panel) and LOS magnetogram (bottom panel) taken by *SDO*/HMI on May 19 at 13:34 UT and centered on the studied AR. Values of the LOS component of the magnetic field are saturated at $\pm$500 G. The black and blue boxes indicate the FoV of the IBIS and *IRIS* observations analyzed in our study, respectively, while the red box shows the ROI where the studied brightening events occur. Here and in the following figures, solar north is to the top, and west is to the right. The horizontal velocity estimated with FLCT is overplotted on the LOS magnetogram. The white reference arrow indicates a horizontal velocity of plasma of 1 km s^{-1}. See Sections 2 and 3 for more details.

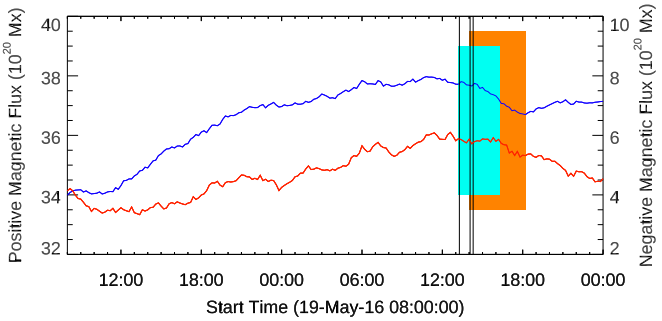

Figure 2. Evolution of positive (red) and negative (blue) magnetic flux in the ROI (marked with the red box in Figure 1) as derived from *SDO*/HMI measurements. The time interval of the *IRIS* sit-and-stare scan and of the IBIS observations is indicated with blue and orange strips, respectively. The vertical lines indicate the three brightening events discussed in the text.

evolution described above and the diverse MMFs discussed below.

The penumbra had a rather homogeneous structure with field inclination of about 60°–90° (Figure 3, third column), except for a few elongated patches with field inclination in the range 40°–60° (marked with the white oval in Figure 3, panels (c3)–(c7)) in the area that broke away. These features were clearly linked to the positive polarity patches of the EFR. The region also displayed two systematic flow patterns, which are shown in Figure 3 (fourth column). The former, directed toward the first EFR, led to the formation of N_3 by the merging of N_1 and N_2, while the second southern-ward pattern contributed to the evolution of the small-scale positive polarity features. Note that the emergence of both EFRs was characterized by strong shear motions with values of the horizontal velocity of the plasma of about 1 km s^{-1}.

The IBIS data provide a close-up view of the evolution of the ROI and of the physical properties therein. In particular, we show in Figure 4 the analyzed area from the IBIS observations taken on 2016 May 20 at 14:00 UT (left panels) and 17:00 UT (right panels), along with results from their inversion. The IBIS data at 14:00 UT indicate that the bright gap in the penumbra (yellow oval) already noticed in the *SDO*/HMI observations separates filaments with different orientation in the irregularly shaped penumbral sector. The dark structures (red arrow), whose length was of about 10″, decreased in size over time until they were no longer detected, e.g., on 2016 May 20 at 18:00 UT. Noticeably, the plasma LOS velocity in small-scale patches of these structures was opposite with respect to the regular Evershed flows nearby (Figure 4 panel (c)).

Figure 4 (panels (d)–(e)) also displays filaments at the atmospheric height $\log \tau = -1.0$ with average values of the field strength and inclination of about 1.4 kG and about 45°, respectively, in the area that broke away from the penumbra, compared to the values for the same quantities of 0.9 kG and 80° for the homogeneous filaments nearby. Later, e.g., at 17:00 UT, the field pattern in the region was unchanged but for the slightly larger extension of the inhomogeneous patches.

3.2. Signatures from the Chromosphere to the Corona

At the chromospheric heights sampled by the IBIS Ca II 854.2 nm measurements, the ROI showed a bundle of filaments with intense and repeated brightening at various locations, especially in the area of the two EFRs. These small-scale enhancements were observed in the form of either circular or elongated features (see the online animation of the Ca II line core images in Figure 4). Moreover, at $\log \tau = -4.6$ (Figure 4, panels (f)–(g)) the ROI exhibited average values of the field strength of about 0.9 kG and field inclination ranging from 60° to 100°, except for some small-scale patches in the inhomogeneous area with field inclination lower than 40°.

The transients observed in IBIS Ca II data were also manifested in the evolution of the average intensity measured over the ROI in the *IRIS* I1400, *SDO*/AIA, and *Hinode*/XRT observations. Figure 5 compares the light curves derived from the above data for the time interval of simultaneous IBIS and *IRIS* data, along with the variation of the X-ray flux measured by the *GOES*-15 satellite (Bornmann et al. 1996).

All the light curves shown in Figure 5 display a couple of remarkable intensity increases standing out with respect to long-term and smooth variations. In particular, we considered the three abrupt intensity changes marked with vertical dashed lines in Figure 5 and referred to in the following as E1, E2, and E3. Two of these peaks, specifically E2 and E3, had clear counterparts in the variation of the X-ray flux measured by *GOES*-15 (red curve in Figure 5) and correspond to B-class flares. The above intensity increases, which lasted a few minutes for all the considered data, had different amplitudes depending on the event and wavelength, see, e.g., the peak value for the E2 and E3 events.

In an attempt to localize the source regions and to investigate the possible trigger mechanisms of the above events, Figure 6 displays *SDO*/HMI, *SDO*/AIA, and *IRIS* data taken over the time interval considered in Figure 5. The various panels in Figure 6 show brightening events whose footpoints and emission contours are overplotted on the I2832 observations for ease of comparison. We clearly noticed two homologous small-scale flaring events developed over a sigmoidal region (panels in the first and third rows of Figure 6). These events correspond to E1 occurring at 13:27 UT and E3 recorded by *GOES*-15 as B-class flares at 14:32 UT, about one hour later than E1. The eastern footpoint of the flaring region was lying in the penumbra, while the other was close to the patch of negative polarity flux N_1. It is worth noting that the latter footpoint can be easily identified in most of the *SDO*/AIA coronal observations that also show an intensity enhancement in the central part of the sigmoidal flaring area during E3. The latter area is only faintly detected in cotemporal chromosphere and TR, see, e.g., I1400 and A304 maps.

Between the above homologous flaring events, we observed the occurrence of E2, a small-scale brightening appeared at about 14:08 UT in the left side of the ROI (panels in the second row of Figure 6) in the form of three elongated small-scale features seen in the A304 and A131 data, and only partly detected in I1400 observations. These bright patches were clearly aligned to penumbral filaments and cospatial to the small-scale positive flux features described in Section 3.1.

We further investigated the differences among E1, E2, and E3 by using I1400 observations, some examples of which are shown in Figure 7. The evolution of E1 was fast (Figure 7, top panels) and with simultaneous signatures seen in the light curves and observations of I1400, A131, and A304. The E2 event lasted about 7 minutes and reached its maximum extension 3 minutes after its start (Figure 7, middle panels) in the form of a bright knot appeared in the penumbra. Three minutes after the first appearance of the bright knot, a thin bright lane connected it to a small bright patch outside the

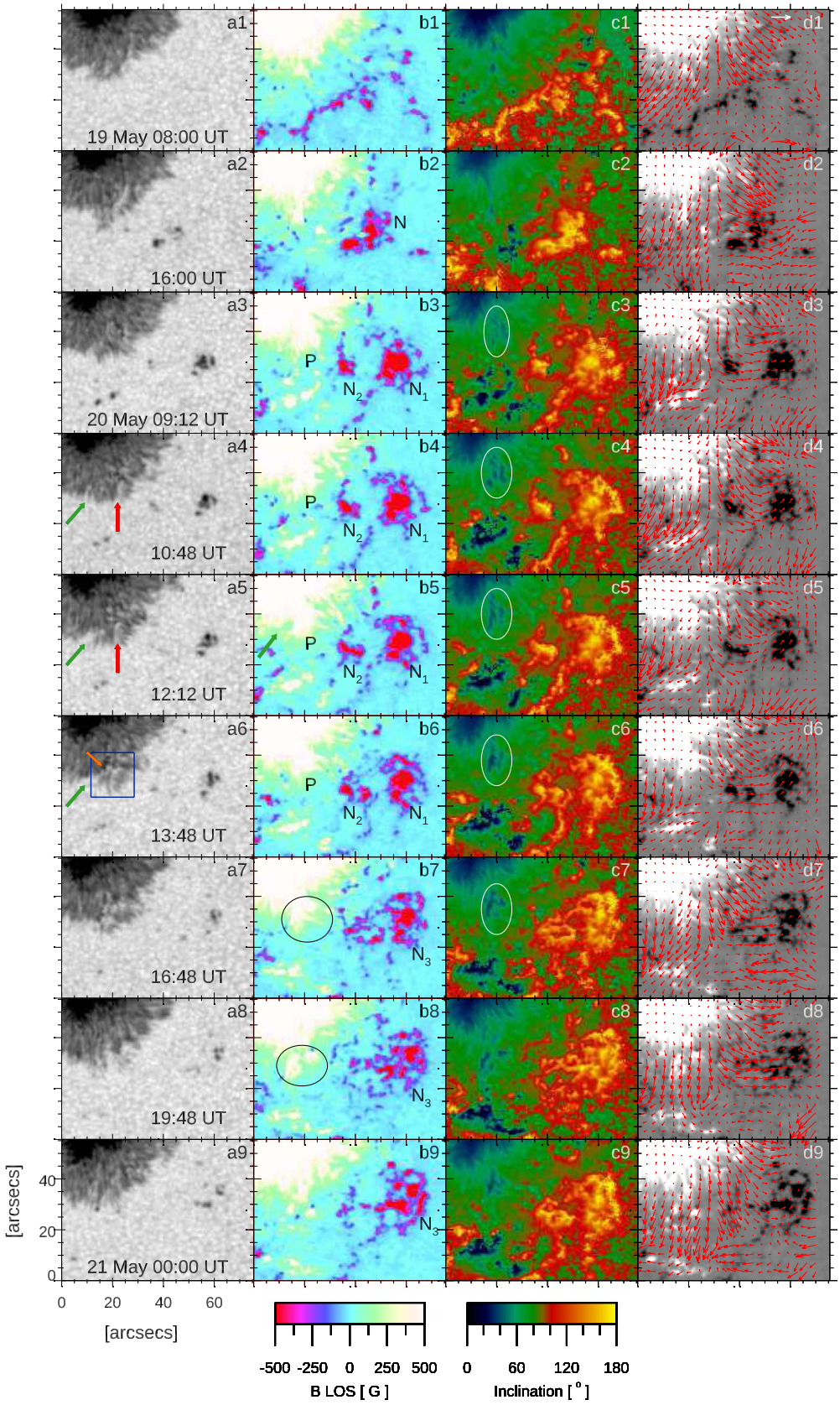

Figure 3. Evolution of the ROI as inferred from *SDO*/HMI data. From left to right, top to bottom: maps of (a) the continuum intensity, (b) LOS magnetic field strength, (c) magnetic field inclination, (d) and plasma horizontal flow velocity for representative times from 2016 May 19 08:00 UT to May 21 00:00 UT that manifest the main changes occurring in the area. Labels, arrows, circles, and ovals overplotted on the maps point to features described in Section 3.1. The blue box in the continuum map taken on May 20 13:48 UT indicates the IBIS sub-FoV shown in Figure 4. The white arrow overplotted in the top-right panel represents a horizontal velocity of 1 km s^{-1}.

(An animation of this figure is available.)

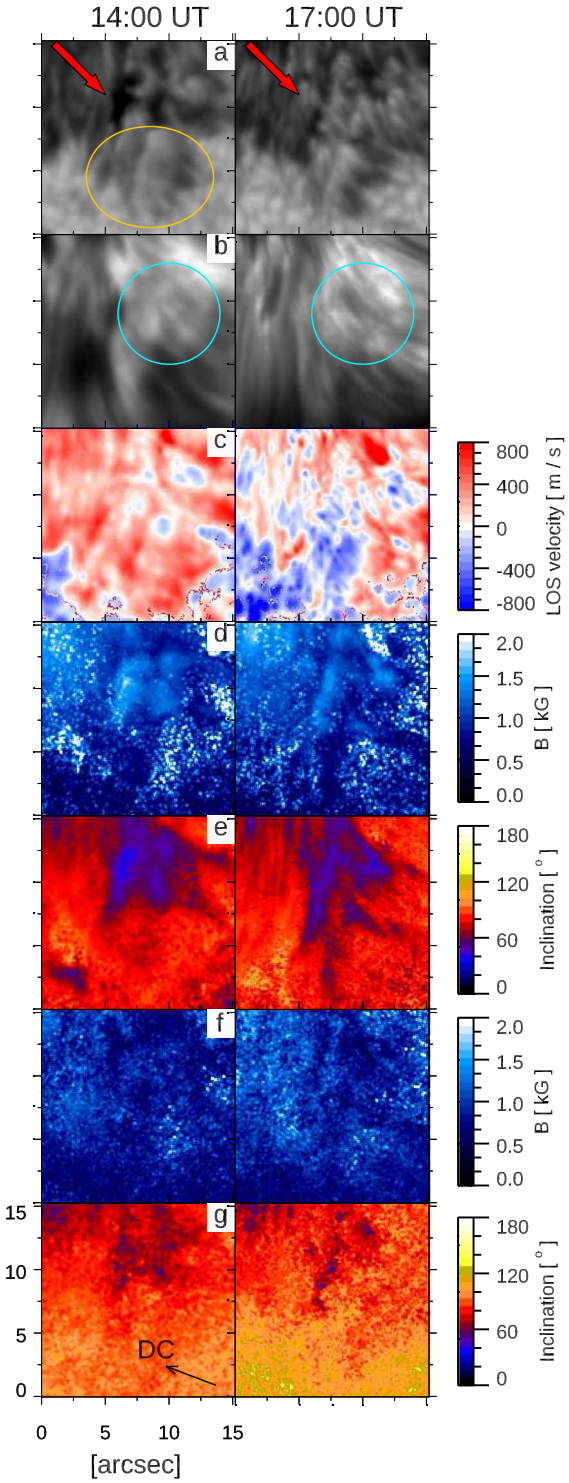

Figure 4. Examples of the IBIS observations analyzed in our study. From top to bottom, the various panels display: maps of (a) the Fe I continuum intensity, (b) Ca II line core intensity, (c) LOS velocity derived from the Doppler shift of the Fe I line center, (d) total magnetic field strength and (e) magnetic field inclination at photospheric height $\log \tau = -1$, (f) total magnetic field strength and (g) magnetic field inclination at the chromospheric height $\log \tau = -4.6$. Downflows and upflows correspond to positive and negative velocity values, respectively. Arrows, ovals, and circles indicate features described in the text. The black arrow in panel (g) points to the disk center. (The animation includes white light images and Ca II line core measurements from all IBIS observations.)

(An animation of this figure is available.)

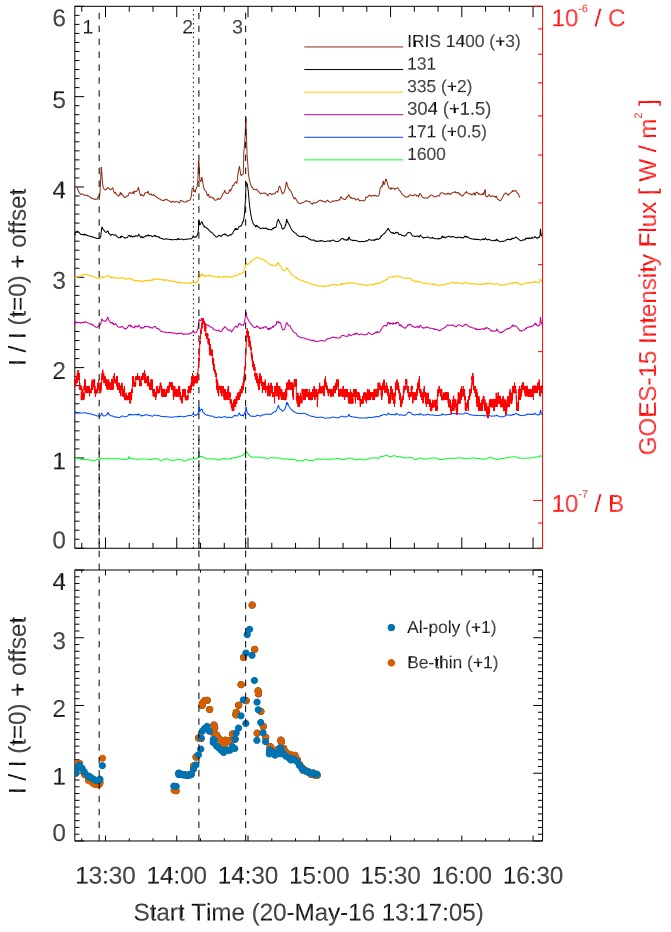

Figure 5. Top panel: Light curves computed from the *SDO*/AIA observations and *IRIS*/SJI 1400 Å data obtained on 2016 May 20 from 13:17 UT to 16:30 UT. The red line represents the X-ray flux measured by *GOES*-15 in the 1–8 Å channel. Note the offsets of the light curves along the y direction, to enhance their visibility. The vertical dotted line indicates the starting time of IBIS observations. The three dashed green lines mark the occurrence of the three brightening events E1, E2, and E3, which are described in Sections 3.2 and 3.3 and shown in Figures 6, 7, and 9. Bottom panel: blue and orange dots represent X-ray light curves obtained from *HINODE*/XRT data through the Al pol and Be thin filters, respectively.

penumbra. This bright lane became brighter with time and reached its maximum extension 4 minutes after its first appearance. E2 produced the strongest signature in the *GOES*-15 X-ray flux record, but only relatively small changes in the intensity emerging from the low chromosphere to the upper TR compared to the same atmospheric layers during E3. The latter transient produced intensity enhancements whose amplitude increased with the atmospheric height. E3 started at 14:20 UT, lasted about 13 minutes, and reached maximum extension (40″) 11 minutes after its beginning. The maximum of intensity in the I1400 data occurred 2 minutes later than recorded for all the *SDO*/AIA EUV channels.

In Figure 8 we show the *Hinode*/XRT X-ray intensity maps acquired during the maximum brightening of E1, E2, and E3 events (second column), as well as 1 minute before (first column) and after (third column) the three events. These images display the same plasma behavior as reported in A131 and the strongest coronal brightening observed during E3 too. In particular, the shape of the E2 brightening (panels (b))

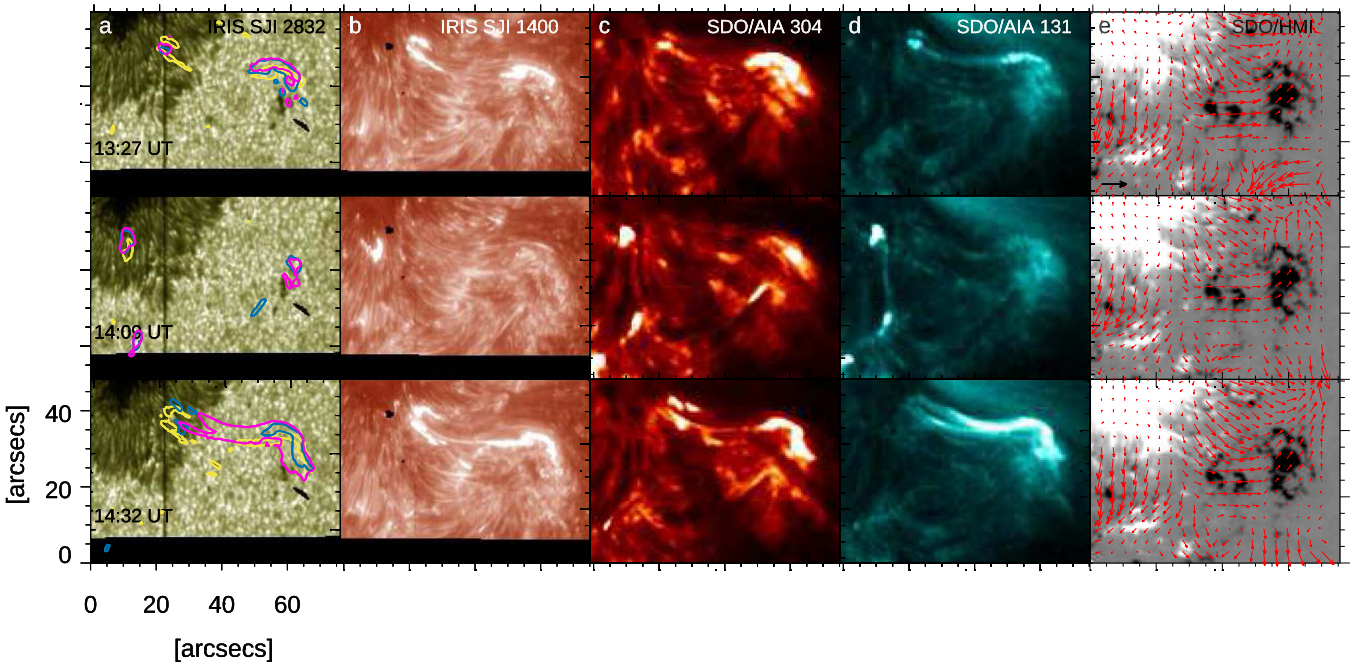

Figure 6. Examples of the *SDO* and *IRIS* data analyzed in our study, relevant to the ROI. From left to right: (a) *IRIS* I2832, (b) *IRIS* I1400, (c) *SDO* A304, and (d) *SDO* A131 filtergrams. Column (e) displays the maps of the LOS magnetic field from *SDO*/HMI data with the horizontal velocity field derived from the same observations overplotted. The light curves in Figure 5 were computed over the FoV shown in these panels. The colored contours overplotted on the *IRIS* I2832 data represent the footpoints and regions of maximum brightening in the *IRIS* I1400 (green), *SDO*/AIA A131 (red), and A304 (blue) measurements, respectively. The black arrow in panel (e) represents a horizontal velocity of 1 km s^{-1}.

indicates the possible connection between opposite polarity patches of the diffuse field and MMF.

3.3. IRIS *Spectra*

The *IRIS* slit sampled the region at $X = [41'']$. We show in Figure 9 examples of the line profiles measured during E1 and E3 at the positions marked by the symbols in Figure 7 in both the inhomogeneous and regular penumbra. From a comparison with Figure 6, we can note that the positions marked with triangles correspond to the eastern footpoints of the flaring loop during both E1 and E3. The red curves represent the spectra measured at the time of maximum brightening of each event. Unfortunately, there are no similar data available for E2.

During the transients, the C II and Si IV line profiles, which are formed in the TR, were enhanced by a factor of about 10 with respect to the line profiles measured in the quiet penumbral region (black curves), taken as a reference. At the time of maximum brightening red curves, the double-peaked C II profiles showed blue lobes stronger than the red ones. In addition, the red wings of the C II intensity profiles were broader than the blue wings. The C II profiles showed asymmetric peaks varying in time, specifically the red lobe stronger than the blue one during the initial stages (blue curve) of the brightening, and opposite peak ranking at the time of maximum brightening (red curve). However, during E3 the C II intensity profile (Figure 9, bottom-left panel) was less asymmetric than reported for E1. The Si IV line profiles during the two events were broadened by a factor of about 3 with respect to that measured in the reference regular penumbra, redshifted, indicating plasma velocities up to about 10 km s^{-1}.

Chromospheric Mg II h&k lines measurements showed a behavior similar to C II spectra, since the double-peaked profiles exhibited blue lobes stronger than the red ones at the peak of the brightening events. Moreover, the emission intensity profiles displayed no significant Doppler shift in all the available data. During the transients, the emission of the Mg II h&k lines was enhanced by a factor 2 with respect to that measured in the regular penumbra. During E1 the profiles were rather symmetric, except for the data taken at maximum brightening (red curve). Conversely, before the E3 transient the profiles displayed red lobes stronger than the blue ones, contrarily to data during the maximum brightening (see blue and red curves in the bottom-right panel of Figure 9).

Noticeably, the Mg II intensity profiles measured during both E1 and E3 showed emission in the Mg II 2798.8 Å triplet (marked by the red arrows in Figure 9).

4. Discussion

We presented our analysis of brightening events observed in the penumbra of AR NOAA 12546. This region included one among the largest sunspots of the solar cycle 24. The data analyzed in our study consist of multiwavelength and multi-instrument measurements obtained with state-of-the-art facilities, specifically with the IBIS, *SDO*/HMI, *SDO*/AIA, *IRIS,* and *Hinode*/XRT instruments. The bright filaments and dark spines forming the penumbra were nearly radially aligned over most of the sunspot structure and during its entire disk passage, except for a small area at a given time. We analyzed the phenomena occurring in this small area at representative times. We found that:

1. A first EFR emerged close to the penumbral field, with a flux content of about 3×10^{20} Mx.
2. The newly emerged flux coalesced to preexisting network field and formed a small pore of opposite polarity flux with respect to the one in the umbra.
3. Another small EFR occurred in the sunspot moat with a flux content of about 5×10^{19} Mx. The negative flux

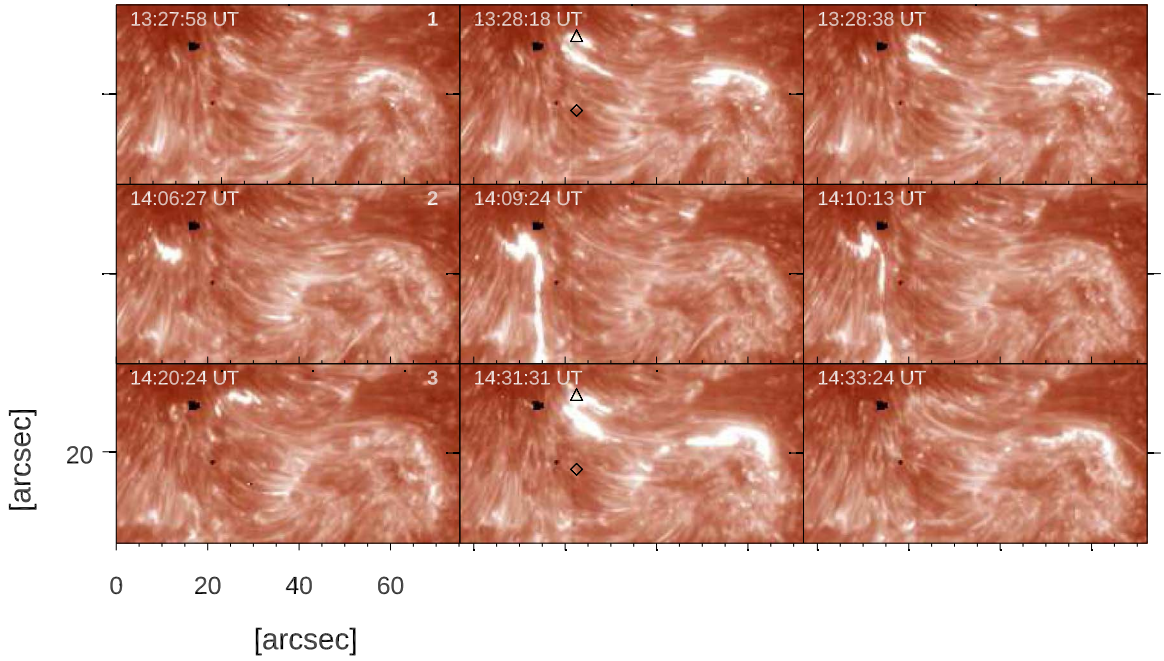

Figure 7. Sequences of *IRIS* I1400 images showing the evolution of the penumbral brightening events labeled as E1, E2, and E3 in Figure 5 and described in Sections 3.2 and 3.3. From left to right, top to bottom: observations taken before, at, and after the maximum brightening of the E1, E2, and E3 events, respectively.

patches from this EFR merged with the pore formed from the previous EFR.

4. During the emergence of the second EFR, a bright gap and some dark patches appeared inside the penumbra, in which the positive polarity of the second EFR was embedded. The bright gap separated filaments with different orientation than the one of the filaments nearby.
5. The above photospheric features were preceded by the formation of elongated patches in the penumbra with magnetic field inclination ranging from 40° to 60°, different with respect to the inclination of the field in the filaments nearby, of about 60°–90°. These elongated patches also showed plasma LOS velocity opposite with respect to the regular Evershed flows nearby.
6. The horizontal plasma flow exhibited two systematic velocity patterns directed from the penumbra toward the first EFR and to the southern side of the ROI. Strong diverging motions with values of the horizontal plasma velocity of about 1 km s^{-1} characterized the area of the two EFRs.
7. Three brightening events occurred during the above evolution of the photospheric magnetic environment, with clear signatures detected from the chromosphere to the corona. All the events had a footpoint located in the penumbra.
8. Two of these events were recorded by *GOES* as B-class flares. One of these (E3) can be also classified as a homologous flare (e.g., Romano et al. 2015), since it showed the same configuration as a previous flaring event (E1). The first homologous flaring event lasted less than the second one. It left simultaneous signatures at all the chromospheric, TR, and coronal analyzed data. The second homologous event lasted about 13 minutes. The flaring region of E3 was about 40″ wide (29 Mm). It is worth mentioning that another homologous flaring event was seen in the *SDO*/AIA filtergrams after the end of the *IRIS* observations, at 16:39 UT.
9. *IRIS* spectra relevant to the penumbral footpoints during the two homologous flares reveal enhanced emission and asymmetries in both the C II and Mg II h&k line profiles, and weak emission at the Mg II 2798.8 Å triplet. In particular, at the time of maximum brightening, the blue lobe profiles are stronger than the red ones.

Observations of AR NOAA 12546 show a large number of short-living MMFs flowing away from the sunspot, some of them occurring in the ROI.

Figure 10 displays the evolution of a few MMFs relevant to the transient brightening events described above. To ease comparison, we overplotted the intensity contours of the studied events on all of the maps in Figure 10. Close to each footpoint of E1, we note type I MMFs (zoomed in the inserts in the left and right corners in Figure 10, panels (a), (b), (c), and (d)).

The MMF at the eastern side streamed out from the penumbra. Eventually, at 13:24 UT, i.e., at the time the E1 occurred, a unipolar feature remained. The MMF at the western footpoint likely underwent a partial magnetic cancellation of the positive flux (see panel (d) in Figure 10), slightly before E1. After E1, we note two couples of type I MMFs (see insert in the left corner of Figure 10, panel (e)) that disappeared at the time of E3. At the western footpoint, the negative flux patch from previous MMF merging was approached by a positive flux feature leading to a partial magnetic flux cancellation event.

The photospheric structures that appeared in the penumbra facing the second EFR had vertical magnetic fields. In the same region we found a bright gap and diverging filaments. We consider these features to be the counterpart of the positive polarity of the EFR, which broke up the uncombed penumbra. This is likely due to the interaction of rising magnetic flux elements with the inclined magnetic field of the penumbra (Ichimoto et al. 2007; Su et al. 2010).

The same regions also exhibited LOS velocity opposite to the Evershed flow observed in the penumbral filaments nearby.

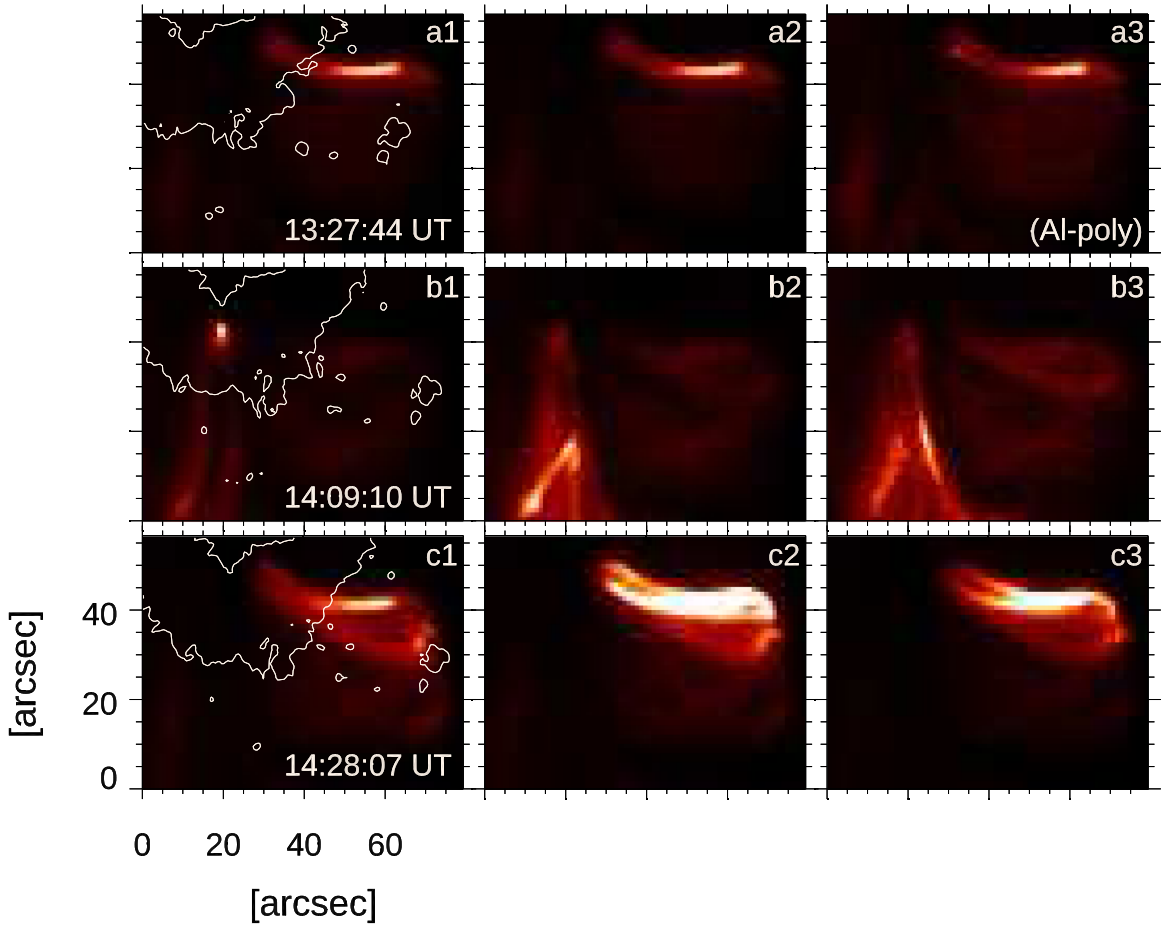

Figure 8. X-ray intensity through the *Hinode*/XRT Be thin filter at the time of E1 (panels (a1)–(a3)), E2 (panels (b1)–(b3)), and E3 (panels (c1)–(c3)) events. The white contours indicate the umbra and penumbra in the continuum intensity as a reference.

We consider that these opposite flows are a further consequence of the above change in the field inclination. Counter Evershed flows were also found in umbral filaments (e.g., Kleint & Sainz Dalda 2013), during the formation of penumbrae (Schlichenmaier et al. 2012; Romano et al. 2014; Murabito et al. 2016, 2018), and over stable penumbrae (Louis et al. 2014; Siu-Tapia et al. 2017).

Lim et al. (2011) presented observations of two granular-like features (GLFs), about 1″ wide, at the tip of penumbral filaments and associated with MMFs. Both the observed GLFs were preceded by elongated darkening and one of these showed fine structure consisting of thin, dark, and bright threads. The two GLFs revealed significant chromospheric transients, specifically brightening in Hα and *SDO*/AIA 1600 Å images and jets. The relatively long-lasting, dark patches we observed in the penumbra were five times wider than reported by the above authors and showed no threads. Besides, the GLFs found by Lim et al. (2011) had opposite polarity to the field in the sunspot umbra, whereas the dark structure observed in our region had the same polarity as the umbral field.

The brightening observed by Bai et al. (2016), about 10″ wide, crossed a penumbra. It started at the border of the penumbra and then elongated toward the umbra, by leaving signatures detected from the chromosphere to the corona. The transient events analyzed in this work differ from the one reported by Bai et al. (2016) mostly for their larger extension and activation over an area that included both the penumbra and moat, as well as for their longer lifetime. Moreover, they do not show any expansion motion.

IRIS spectroscopic information is relevant to the eastern footpoints of events E1 and E3, embedded in the penumbra. According to Rathore et al. (2015), *IRIS* C II intensity profiles are a powerful discriminant of upper chromospheric structures, and their asymmetries and line shifts are a robust velocity diagnostic. They showed that the C II spectral profiles can have a single peak or two or more peaks, depending on how the source function varies with the atmospheric height. They attributed the asymmetry of intensity profiles to velocity gradients between the formation height of the intensity peaks and of the line core. In particular, by comparing the intensity profiles measured in active and quiet Sun regions, Rathore et al. (2015) reported line profiles with the blue peak stronger/weaker than the red one and attributed this profile feature to plasma with downflow/upflow above the peak formation height. In our data, we found: (i) the intensity profiles measured during the initial stages of both events with red peaks stronger than the blue ones, thus revealing plasma upflow at the time of those measurements; (ii) at maximum brightening, intensity profiles with blue peaks stronger than red ones, thus hinting at plasma downflow; (iii) E1 showed a stronger asymmetry of the C II intensity profiles than that derived from E3; (iv) the intensity profiles measured after E3 display blue peaks stronger than red ones, whereas the ones measured after E1 do not clearly show the same feature.

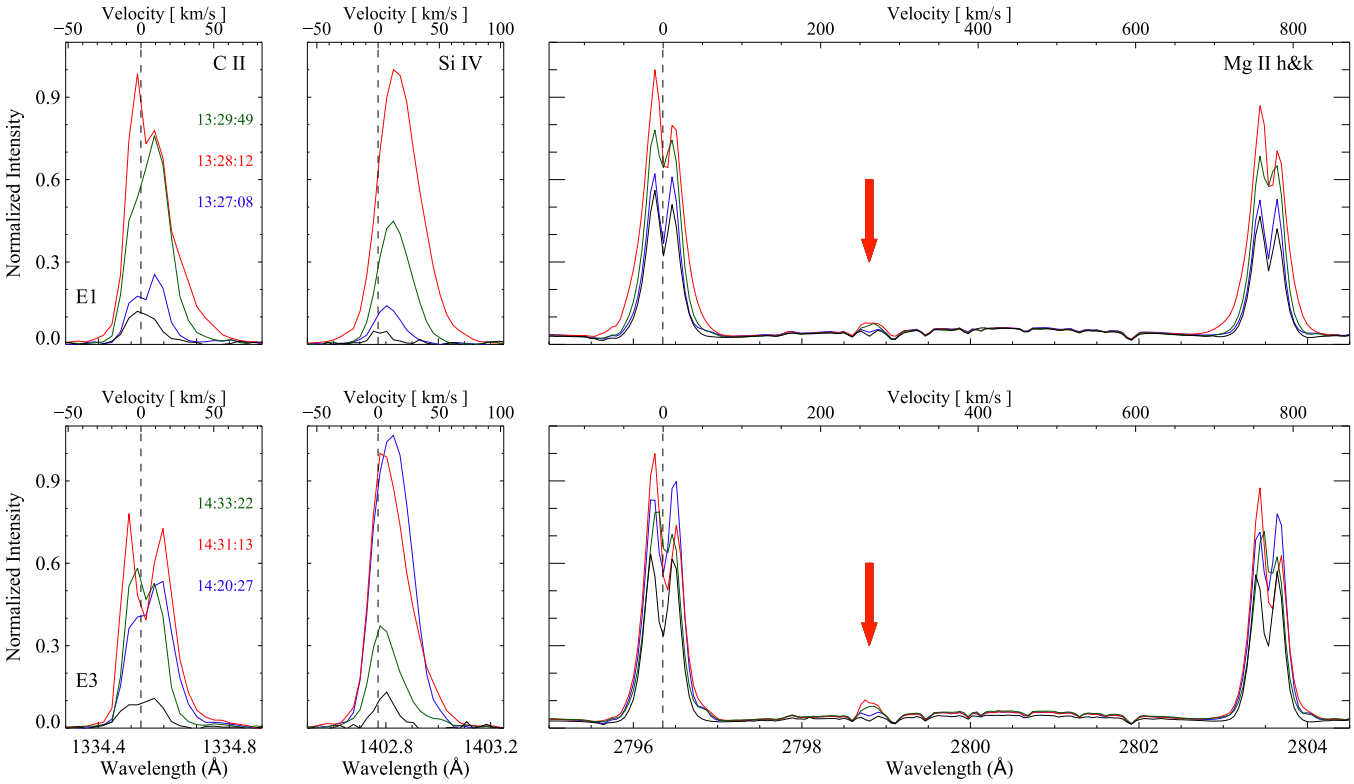

Figure 9. Spectra from *IRIS* observations taken during the E1 (top panels) and E3 (bottom panels) penumbral brightening events. From left to right: profiles of the C II 1334.53 Å, Si IV 1402.77 Å, and Mg II h&k lines at three times during each studied event and in a quiet penumbral region considered as a reference. The line profile of the latter region is shown with a solid black line. Blue, red, and green lines display the measurements taken before, at, and after each brightening, respectively. Red arrows indicate the rare weak emission at the Mg II 2798.8 Å.

The C II spectra of the brightening event reported by Bai et al. (2016) are asymmetric with the red peak stronger than the blue one, in contrast with the observations analyzed in our study.

The intensity profiles of the chromospheric Mg II h&k lines measured during E1 and E3 are also double-peaked but rather symmetric except for the data taken at maximum brightening which have blue peaks stronger than red ones as for plasma downflow at the formation height of the intensity peaks (Leenaarts et al. 2013). Finally, the width of the intensity profiles of the Mg II h&k lines does not change significantly during the studied events as for a temperature increase associated with the brightening not occurring in the lower chromosphere (Pereira et al. 2015). It is worth noting that the Mg II 2796.35 Å intensity profile presented by Bai et al. (2016) is symmetric as expected from quiet plasma at the formation height of the analyzed intensity peak in contrast to our data.

Indeed, we notice that the blue peaks are stronger than the red ones for both the C II and Mg II h&k line data, especially during event E3, which is the stronger brightening. This asymmetry suggests the occurrence of chromospheric evaporation at the penumbral footpoints following a magnetic reconnection process occurring at higher atmospheric heights, as hypothesized by Bai et al. (2016).

Furthermore, the Mg II intensity profiles we measured during both E1 and E3 show a weak emission of Mg II 2798.8 Å triplet. Pereira et al. (2015) attributed this rare emission to a steep temperature increase in the lower chromosphere. The Mg II 2798.8 Å emission can involve either the far wings or core of the line, depending on the range of interested column masses. In particular, the emission seen in the wings of the intensity profile points to plasma heating occurring deeper down the chromosphere than that recorded at the line core, which is suggestive of pure chromospheric heating (Hansteen et al. 2017). Our data show Mg II 2798.8 Å emission in the line core, thus revealing that E1 and E3 produced a steep temperature increase at chromospheric heights.

We also considered the results presented above with respect to the findings of MHD numerical simulations of coronal and chromospheric microflares performed by Jiang et al. (2012). In these numerical models the microflares leave different atmospheric signatures and have different size depending on the atmospheric height of the magnetic reconnection episode responsible for the flaring. In particular, in the case of the simulated coronal microflares, the size of the brightening region ranges from 15″ to 22″. The upper atmosphere response to the event simulated by Jiang et al. (2012) includes both hot plasma jets ($\approx 1.8 \times 10^6$ K) observed in the EUV/X-ray bands and cold jets ($\approx 10^4$ K) revealed as Hα/Ca brightening events. Moreover, the numerical studies indicate a time delay between the signatures of the reconnection process seen in the upper and lower atmosphere. In particular, the enhanced EUV/X-ray emission was found to appear before the Hα/Ca brightening. Jiang et al. (2012) roughly derived an estimate for this time delay. By taking into account the temperature response at 1500 km (the height formation of Hα, Vernazza et al. 1981) those authors reported a time delay of about 3–5 minutes. The spatial scale of the studied brightening events in their signatures in the various layers of atmosphere agree with those reported by the simulation results of Jiang et al. (2012) for coronal microflares.

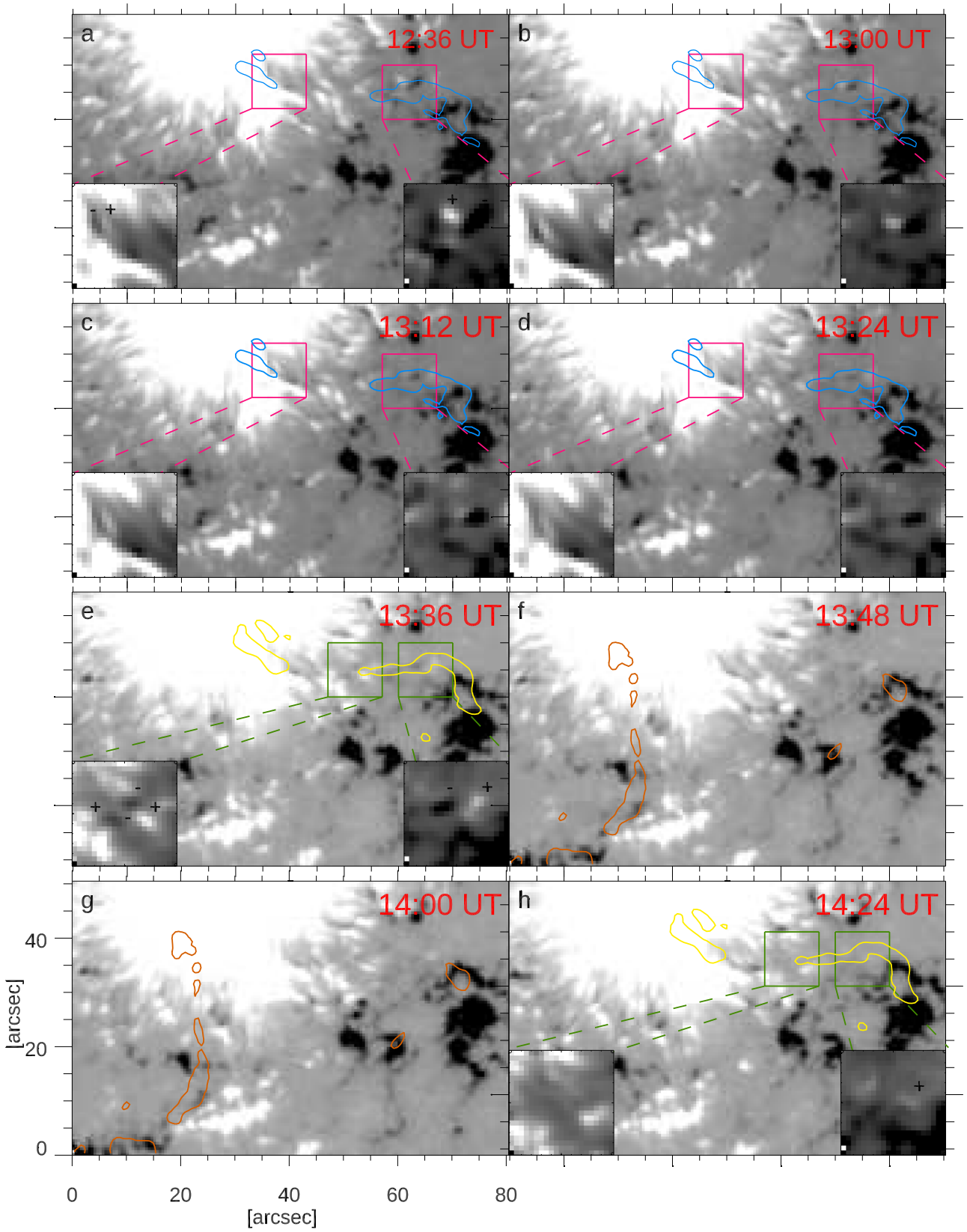

Figure 10. Magnetic evolution of the ROI before the E1 and E3 events. The regions in the pink and green squares are shown zoomed in the inserts at the left and right corners of each panel. The light blue, orange, and yellow contours mark the intensity pattern at maximum brightening in *SDO*/AIA A304 for E1, E2, and E3, respectively. The polarities of the MMFs identified in the inserts are shown by the "+" and "–" symbols.

We have seen that the magnetic configuration analyzed in Figure 10 for the three penumbral brightenings suggest a clear link between the EFR, MMFs, and the preexisting penumbral field. In regard to the trigger mechanism of the observed transient events, E1 and E3 seem due to the interaction between the penumbral fields and the EFR. In particular, the outer

negative footpoint of the EFR interacts with the MMFs departing from the penumbra, as suggested in the model proposed by Kano et al. (2010; flux emergence case). Moreover, the positive footpoint of the EFR inside the penumbra also comes into contact with negative polarities around the penumbra originated by either MMFs or flux return patches. This interaction may activate magnetic reconnection events. On the other hand, E2 seems due to the interplay between MMFs and the preexisting diffuse field to the south of the sunspot, as suggested by the crossing enhanced connections visible in the *Hinode*/XRT images. This is reminiscent of the model introduced by Kano et al. (2010; MMFs interaction case). Therefore, for the three studied events there is a tight distinctive interplay among EFR, MMFs, and preexisting magnetic flux systems.

5. Conclusions

In this paper, we analyzed multiwavelength observations of the AR NOAA 12546 obtained with state-of-the-art instruments to further investigate the trigger mechanism of penumbral brightening events. In particular, we studied the evolution of the AR penumbral area adjacent to two small-scale EFRs that emerged in the AR on 2016 May 20. The analyzed region showed three brightening events detected from the chromosphere to the corona. From analysis of IBIS, *SDO*/HMI, *SDO*/AIA, *IRIS*, and *Hinode* observations we found that two of the studied events likely derived from reconnection processes occurring at different atmospheric heights that were activated by the interaction of the preexisting fields with either the EFRs or MMFs.

Penumbral transient brightening events have been attributed to magnetic reconnection processes occurring in the low corona (Bai et al. 2016). The spatial scale of the events analyzed in our study in their signatures in the atmosphere agree with those reported by the simulation results of Jiang et al. (2012) for coronal microflares. Moreover, our observations confirm the model for nanoflare events sketched in Figure 12 of the paper by Kano et al. (2010), both for the flux emergence and MMFs interaction cases. They also complement the results presented by Bai et al. (2016) showing the signatures of the chromospheric evaporation following the flaring events not found by those authors.

We plan to further analyze penumbral brightening events to understand the role of the less energetic occurrences in the heating of the chromosphere and upper atmosphere. Spectropolarimetric observations to accurately infer the vector magnetic field at different heights in the solar atmosphere, and simultaneous images and spectra from the photosphere outward, such as those expected by the upcoming new generation solar observatories (DKIST, Tritschler et al. 2015; *Solar Orbiter*, Müller et al. 2013) are essential to perform these studies.

The authors wish to thank the anonymous referee for helpful comments. The authors are grateful to Doug Gilliam for the IBIS observations analyzed in this study. S.L.G. and M.M. wish to thank Peter Young for useful discussion. This work has received funding from the European Union's Horizon 2020 research and Innovation program under grant agreements No. 739500 (PRE-EST) and No. 824135 (SOLARNET). S.L.G. acknowledges support from the Università degli Studi di Catania (Piano per la Ricerca Università di Catania 2016–2018—Linea di intervento 1 "Chance"; Linea di intervento 2 "Ricerca di Ateneo—Piano per la Ricerca 2016/2018"). This research has made use of NASA's Astrophysics Data System. *IRIS* is a NASA small explorer mission developed and operated by LMSAL with mission operations executed at NASA Ames Research center and major contributions to downlink communications funded by the Norwegian Space Center (NSC, Norway) through an ESA PRODEX contract.

ORCID iDs

Mariarita Murabito https://orcid.org/0000-0002-0144-2252
Salvo L. Guglielmino https://orcid.org/0000-0002-1837-2262
Ilaria Ermolli https://orcid.org/0000-0003-2596-9523
Marco Stangalini https://orcid.org/0000-0002-5365-7546

References

Archontis, V. 2012, RSPTA, 370, 3088
Archontis, V., Moreno-Insertis, F., Galsgaard, K., et al. 2004, A&A, 426, 1047
Bai, X. Y., Su, J. T., Cao, W. D., et al. 2016, ApJ, 823, 60
Balthasar, H. 1988, A&A, 72, 473S
Benz, A. O. 2017, LRSP, 14, 2
Bharti, L., Hirzberger, J., & Solanki, S. K. 2013, A&A, 552, L1
Bobra, M. G., Sun, X., Hoeksema, J. T., et al. 2014, SoPh, 289, 3549
Bornmann, P. L., Speich, D., Hirman, J., et al. 1996, Proc. SPIE, 2812, 309
Borrero, J. M., & Ichimoto, K. 2011, LRSP, 8, 4
Cao, W., Gorceix, N., Coulter, R., et al. 2010, AN, 331, 636
Cavallini, F. 2006, SoPh, 236, 415
Chen, F., & Ding, M. D. 2010, ApJ, 724, 640
Cheung, M. C. M., & Isobe, H. 2014, LRSP, 11, 3
Criscuoli, S., Del Moro, D., Giannattasio, F., et al. 2012, A&A, 546, A26
De Pontieu, B., Title, A. M., Lemen, J. R., et al. 2014, SoPh, 289, 2733
Dravins, D., Lindergren, L., & Nordlund, Å. 1981, A&A, 96, 345
Ermolli, I., Cristaldi, A., Giorgi, F., et al. 2017, A&A, 600, A102
Fisher, G. H., & Welsch, B. T. 2008, in ASP Conf. Ser. 383, Subsurface and Atmospheric Influences on Solar Activity, ed. R. Howe et al. (San Francisco, CA: ASP), 373
Fontenla, J. M., Avrett, E. H., & Loeser, R. 1993, ApJ, 406, 319
Galsgaard, K., Archontis, V., Moreno-Insertis, F., et al. 2007, ApJ, 666, 516
Galsgaard, K., Moreno-Insertis, F., Archontis, V., et al. 2005, ApJL, 618, L153
Golub, L., Deluca, E., Austin, G., et al. 2007, SoPh, 243, 63
Goode, P. R., Coulter, R., Gorceix, N., et al. 2010, AN, 331, 620
Graham, D. R., & Cauzzi, G. 2015, ApJL, 807, L22
Guglielmino, S. L. 2012, in ASP Conf. Ser. 455, 4th Hinode Science Meeting: Unsolved Problems and Recent Insights, ed. L. R. Bellot Rubio, F. Reale, & M. Carlsson (San Francisco, CA: ASP), 109
Guglielmino, S. L., Bellot Rubio, L. R., Zuccarello, F., et al. 2010, ApJ, 724, 1083
Guglielmino, S. L., Young, P. R., & Zuccarello, F. 2019, ApJ, 871, 82
Guglielmino, S. L., Zuccarello, F., Young, P. R., et al. 2018, ApJ, 856, 127
Hansteen, V. H., Archontis, V., Pereira, T. M. D., et al. 2017, ApJ, 839, 22
Ichimoto, K., Suematsu, Y., Tsuneta, S., et al. 2007, Sci, 318, 1597
Jiang, R.-L., Fang, C., & Chen, P.-F. 2012, ApJ, 751, 152
Kano, R., Shimizu, T., & Tarbell, T. D. 2010, ApJ, 720, 1136
Kleint, L., & Sainz Dalda, A. 2013, ApJ, 770, 74
Kosugi, T., Matsuzaki, K., Sakao, T., et al. 2007, SoPh, 243, 3
Leenaarts, J., Pereira, T. M. D., Carlsson, M., et al. 2013, ApJ, 772, 90
Lemen, J. R., Title, A. M., Akin, D. J., et al. 2012, SoPh, 275, 17
Li, Q., Deng, N., Jing, J., et al. 2019, ApJ, 876, 129
Lim, E.-K., Yurchyshyn, V., Abramenko, V., et al. 2011, ApJ, 740, 82
Löfdahl, M. G. 2002, Proc. SPIE, 4792, 146LS
Louis, R. E., Beck, C., Mathew, S. K., & Venkatakrishnan, P. 2014, A&A, 570, A92
Louis, R. E., Kliem, B., Ravindra, B., et al. 2015, SoPh, 290, 3641
MacTaggart, D., Guglielmino, S. L., Haynes, A. L., et al. 2015, A&A, 576, A4
Müller, D., Marsden, R. G., St., Cyr, O. C., et al. 2013, SoPh, 285, 25
Murabito, M., Ermolli, I., Giorgi, F., et al. 2019, ApJ, 873, 126
Murabito, M., Romano, P., Guglielmino, S. L., Zuccarello, F., & Solanki, S. K. 2016, ApJ, 825, 75, 7
Murabito, M., Zuccarello, F., Guglielmino, S. L., & Romano, P. 2018, ApJ, 855, 58
Pereira, T. M. D., Carlsson, M., De Pontieu, B., & Hansteen, V. 2015, ApJ, 806, 14

Pesnell, W. D., Thompson, B. J., & Chamberlin, P. C. 2012, SoPh, 275, 3
Peter, H., Tian, H., Curdt, W., et al. 2014, Sci, 346, 1255726
Priest, E., & Forbes, T. 2000, in Magnetic Reconnection, ed. E. Priest & T. Forbes (Cambridge: Cambridge Univ. Press), 612
Rathore, B., Carlsson, M., Leenaarts, J., & De Pontieu, B. 2015, ApJ, 811, 81
Rempel, M., & Schlichenmaier, R. 2011, LRSP, 8, 3
Romano, P., Guglielmino, S. L., Cristaldi, A., et al. 2014, ApJ, 784, 10
Romano, P., Zuccarello, F., Guglielmino, S. L., et al. 2015, A&A, 582, A55
Scharmer, G. B., Bjelksjo, K., Korhonen, T. K., Lindberg, B., & Petterson, B. 2003, Proc. SPIE, 4853, 341
Scherrer, P. H., Schou, J., Bush, R. I., et al. 2012, SoPh, 275, 207
Schlichenmaier, R., Rezaei, R., & Bello González, N. 2012, in ASP Conf. Ser. 455, 4th Hinode Science Meeting: Unsolved Problems and Recent Insights, ed. L. Bellot Rubio, F. Reale, & M. Carlsson (San Francisco, CA: ASP), 61
Schmieder, B., Archontis, V., & Pariat, E. 2014, SSRv, 186, 227
Shibata, K., & Magara, T. 2011, LRSP, 8, 6
Siu-Tapia, A., Lagg, A., Solanki, S. K., van Noort, M., & Jurčák, J. 2017, A&A, 607, A36
Socas-Navarro, H., de la Cruz Rodríguez, J., Asensio Ramos, A., Trujillo Bueno, J., & Ruiz Cobo, B. 2015, A&A, 577, A7
Stangalini, M., Jafarzadeh, S., Ermolli, I., et al. 2018, ApJ, 869, 110
Su, J., Liu, Y., Zhang, H., et al. 2010, ApJ, 710, 170
Testa, P., De Pontieu, B., Allred, J., et al. 2014, Sci, 346, 1255724
Tian, H., Li, G., Reeves, K. K., et al. 2014, ApJL, 797, L14
Tritschler, A., Rimmele, T. R., Berukoff, S., et al. 2015, in 18th Cambridge Workshop on Cool Stars, Stellar Systems, and the Sun, ed. G. van Belle & H. C. Harris (Flagstaff, AZ: Lowell Observatory), 933
Tsuneta, S., Ichimoto, K., Katsukawa, Y., et al. 2008, SoPh, 249, 167
Vernazza, J. E., Avrett, E. H., & Loeser, R. 1981, ApJS, 45, 635
Zuccarello, F., Romano, P., Guglielmino, S. L., et al. 2009, A&A, 500, L5